

# Structure–Activity Relationships for the Affinity of Chaotropic Polyoxometalate Anions towards Proteins

Albert Solé-Daura,<sup>[a]</sup> Josep M. Poble, <sup>[a]</sup> and Jorge J. Carbó\*<sup>[a]</sup>

[a] A. Solé-Daura, Prof. Dr. J. M. Poble, Dr. J. J. Carbó  
Departament de Química Física i Inorgànica  
Universitat Rovira i Virgili  
Marcel·lí Domingo 1, 43007 Tarragona, Spain  
E-mail: j.carbo@urv.cat

Supporting information for this article is given via a link at the end of the document.

**Abstract:** The influence of the composition of chaotropic polyoxometalate (POM) anions into their affinity to biological systems was studied by means of atomistic Molecular Dynamics (MD) simulations. The variations in the affinity to hen egg–white lysozyme (HEWL) were analyzed along two series of POMs whereby the charge or the size and shape of the metal cluster are modified systematically. Our simulations revealed a quadratic relationship between the charge of the POM and its affinity to HEWL as a consequence of the parabolic growth of POM···water interaction with the charge. As the charge increases POMs become less chaotropic (more kosmotropic) increasing the number and the strength of POM–water hydrogen bonds and structuring the solvation shell around the POM. This atomistic description explains the proportionally larger desolvation energies and less protein affinity for highly charged POMs, and consequently, the preference for moderate charge densities ( $q/M = 0.33$ ). Also, our simulations suggest that POM···protein interactions are size-specific. The cationic pockets of HEWL protein show a preference for Keggin–like structures, which display the optimal dimensions (~1 nm). Finally, we developed a quantitative multidimensional model for protein affinity with predictive ability ( $r^2 = 0.97$ ;  $q^2 = 0.88$ ) using two molecular descriptors that account for the charge density (charge per metal atom ratio;  $q/M$ ) and the size and shape (shape weighted–volume;  $V_S$ ).

## Introduction

Polyoxometalates (POMs) constitute a family of anionic polynuclear metal oxide clusters that are usually built up from early transition metal ions such as W, Mo or V in their highest oxidation state.<sup>[1],[2]</sup> Due to their structural variability, facile tuneability and outstanding properties, including high stability under oxidizing or hydrolytic conditions, high thermal stability and redox activity, POMs have been largely employed in material science<sup>[3]</sup> and catalysis.<sup>[4]</sup> More significant for this work is their promising application in the fields of biochemistry and chemical medicine.<sup>[5]</sup> These disciplines take benefit from, among others, the *in vitro* and *in vivo* antiviral, antibacterial or antitumor properties that POMs have shown to possess.<sup>[6]–[8]</sup> In addition, POMs have been extensively used in protein crystallography for phasing or as crystallization additives.<sup>[9]</sup> Notably, Yonath and co–workers were able to determine the crystal structure of the ribosome subunits using POMs as “super–heavy atoms” that were tightly attached on the ribosome surface facilitating its crystallization.<sup>[10]</sup> Furthermore, Parac–Vogt and co–workers have reported during the last decade the use of POMs as artificial metalloproteases. Zr-, Ce, and Hf-substituted POM

structures were applied to the hydrolysis of small di– and tripeptide substrates<sup>[11]</sup> and more importantly, to the selective hydrolysis of a wide range of proteins.<sup>[12]–[15]</sup>

It is widely accepted that the biological activity of POMs depends largely on their ability to establish non-bonding interactions with peptides and proteins.<sup>[16]</sup> In turn, these interactions were recognized to be influenced by the electrostatic charge of the POM, its size and shape in host–guest interactions, and its composition.<sup>[13]–[28]</sup> Recently, the affinity of POMs towards biomolecules have been attributed to the *superchaotropic* character of the POM anion, providing a broader description of the physicochemical foundations of POM–protein interactions.<sup>[17]</sup> In chaotropic anions, typically large and charge-delocalized, the ion–dipole interaction with the solvent is less directional, and therefore, the desolvation process upon binding does not change the bulk water structure in large extent reducing the entropy penalty. For example, Nadjo and co–workers found this thermodynamic fingerprint in the binding of Keggin [H<sub>2</sub>W<sub>12</sub>O<sub>40</sub>]<sup>6-</sup> anion to human serum albumin (HSA) protein, where the binding reaction is enthalpically driven ( $\Delta H = -50 \text{ kJ}\cdot\text{mol}^{-1}$ ) with a small, unfavourable entropy component ( $T\Delta S = -12 \text{ kJ}\cdot\text{mol}^{-1}$ ) due to the minimal dehydration entropy change.<sup>[18]</sup> Furthermore, Molitor et al. proposed even an entropic gain upon binding the [TeW<sub>6</sub>O<sub>24</sub>]<sup>6-</sup> anion to proteins.<sup>[29]</sup>

Several attempts to set empirical structure–activity trends relating the activity of POMs to their composition have been reported in the literature.<sup>[13],[15],[18],[19],[23],[24],[27],[28]</sup> Among them, we highlight a very recent study by Rompel *et al.* that investigates systematically the inhibition of mushroom tyrosidase *ab*PP04 by a series of structurally related Keggin–type anions, aiming to set charge–dependent activity correlations.<sup>[28]</sup> However, in general, due to limitations in POM stability under experimental conditions, the number of structures available for setting clear relationships is limited, and they do not provide a whole, unambiguous picture. It is also common that tested POMs differ in more than one feature at a time, hampering the interpretation of the results. In this regard, computational modelling would allow performing systematic variations on single parameters of well-defined POM structures and thus making possible this type of fundamental studies. In a previous contribution, we provided a computational, atomistic description of the POM–protein interactions based on molecular dynamics simulations (MD).<sup>[30]</sup> The study was backed by experimentally reported systems formed by model hen egg–white lysozyme (HEWL) protein and experimentally reported Ce<sup>IV</sup>– and Zr<sup>IV</sup>–substituted POMs,<sup>[31]–[33]</sup> as well as, Te<sup>VI</sup>–centred

POM.<sup>[34]</sup> Simulation revealed that POMs interact mainly with the side chains of the positively charged and polar uncharged residues via charge attraction and hydrogen bonding of the basic oxygen atoms of POM framework.<sup>[30]</sup> Then, Prabhakar and co-workers have computationally characterized interactions of the same nature between POMs and HSA protein.<sup>[35]</sup>

Herein, we study how the affinity to HEWL protein varies along two series of POMs in which the charge and the size of the POM are systematically modified (Figure 1). Aiming to understand the influence of each individual POM feature, we analyze at atomic level the interaction of POMs with both the protein and the solvent. Finally, we build multidimensional correlation between the POM structure and its protein affinity by using two molecular descriptors: the charge per metal ratio ( $q/M$ )<sup>[28],[36]</sup> and the novel descriptor *shape-weighted volume* ( $V_S$ ).

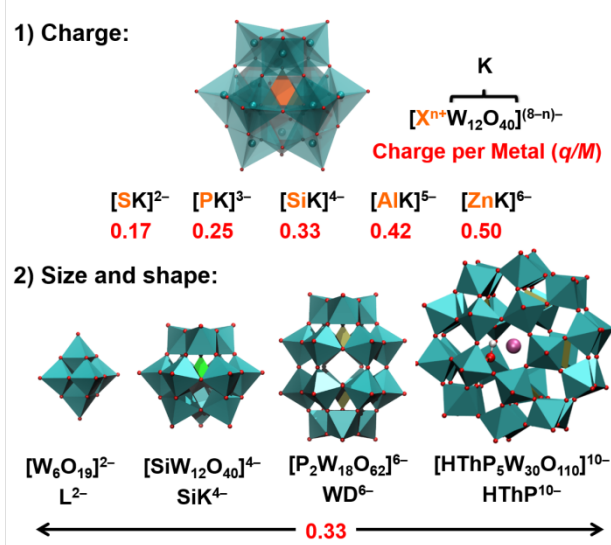


**Figure 1.** Polyhedral representation of the model POM structures used to evaluate the influence of the charge (top) and the size and shape (bottom) of the POM on POM⋯protein interactions.

## Results and Discussion

### Influence of the POM charge.

To understand how the POM charge affects their interaction with proteins, we initially simulated HEWL protein in solution with five different POMs of the same size and shape but different overall charges. The selected POM structures are represented in Figure 1 (top) and comprise five Keggin-like anions of general formula  $[\text{X}^{n+}\text{W}_{12}\text{O}_{40}]^{(8-n)-}$  with  $\text{X}^{n+} = \text{S}^{\text{VI}}, \text{P}^{\text{V}}, \text{Si}^{\text{IV}}, \text{Al}^{\text{III}}$  and  $\text{Zn}^{\text{II}}$ , labeled as  $\text{SK}^{2-}$ ,  $\text{PK}^{3-}$ ,  $\text{SiK}^{4-}$ ,  $\text{AlK}^{5-}$  and  $\text{ZnK}^{6-}$ , respectively. This array of POMs allowed covering a range of charges from 2−, for the least charged  $\text{SK}^{2-}$  to 6− for  $\text{ZnK}^{6-}$ . For every polyoxoanion, we performed a set of five independent MD runs of 20 ns each. The POM trajectories are graphically represented in the Supporting Information (Figure S1) as color evolution of their center of mass around the protein.

To illustrate the specific interactions of Keggin anions with positively charged and polar amino acids of HEWL, we selected the archetypal  $\text{PK}^{3-}$  anion. The volumetric density map in Figure

2A represents the protein regions interacting with the POM, which mostly involve positively charged amino acids such as arginines and lysines. Notably, the two binding sites containing Arg21 and Arg45, respectively, had been actually observed in crystal X-ray structures of noncovalent complexes with different transition metal-substituted Keggin and Wells-Dawson anions.<sup>[31],[33]</sup> In addition, these two positive patches on the protein surface were related to the selective peptide bond hydrolysis catalyzed by Lewis acid metal-substituted POMs.<sup>[12],[30]</sup> X-ray studies have identified an additional binding site containing Arg128, which is placed at a C-terminus end of the HEWL protein.<sup>[31],[33]</sup> This is an unstructured region of the protein, whose interaction with the POMs was suggested to induce a higher degree of structural stability in the solid state,<sup>[33]a</sup> explaining why the interaction of  $\text{PK}^{3-}$  anion is scarcely observed in the simulations in solution. Figure 2B shows a selected snapshot with representative interactions between the oxygen atoms of POM framework and the amino acids of HEWL. As it had been computationally characterized<sup>[30]</sup> and experimentally observed,<sup>[31]-[33]</sup> the nature of these interactions comprises mainly electrostatic interactions, hydrogen bonding and water-mediated interactions with positively-charged and polar amino acids.

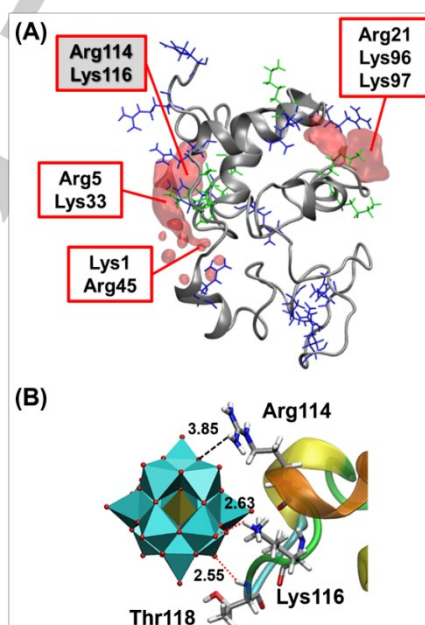


**Figure 2.** A) Volumetric density of the  $\text{PK}^{3-}$  contacts on the protein surface (POM⋯protein distance  $\leq 3.5$  Å) averaged over 100 ns of MD trajectories. Positively charged arginine and lysine residues are depicted in blue and green sticks, respectively. B) Typical snapshot of the interaction of  $\text{PK}^{3-}$  at a positively charged patch on HEWL surface, comprising Arg114, Lys116, and Thr118. Red dotted lines and black dashed lines represent H-bonds and purely electrostatic contacts, respectively. Distances in Å.

Inspection of the trajectories reveals well-differentiated behaviors of POMs over the protein surface (see Figure S1). Depending on the charge, the anion is set in a specific cationic pocket or it moves over the protein surface and in and out of the solution. To evaluate the affinity of the POMs to the protein, the persistence of POM⋯protein contacts was quantified in terms of % *time binding*. This parameter was calculated for each individual POM anion as the number of snapshots in which the

POM is closer than 3.5 Å to the protein and normalized by the total number of snapshots.<sup>[30]</sup> Figure 3 plots the computed values of % *time binding* as a function of POM charge and Table 1 collects the numerical values. The % *time binding* follows the same trend as the peak integration of POM units in the radial distribution function (RDF) between the POM and protein surface (see Figure S2), further supporting the use of this descriptor for evaluating POM affinity.

**Table 1.** Comparison of the HEWL affinity, and the protein and solvent interactions for the five Keggin-type POMs.<sup>[a]</sup>

anion	% <i>time binding</i>	$E_{\text{POM}\cdots\text{HEWL}}$	$E_{\text{POM}\cdots\text{water}}$	H-bonds 1 <sup>st</sup> shell
[SW <sub>12</sub> O <sub>40</sub> ] <sup>2-</sup> (SK <sup>2-</sup> )	72.0	-360	-572	7.3
[PW <sub>12</sub> O <sub>40</sub> ] <sup>3-</sup> (PK <sup>3-</sup> )	88.9	-571	-823	9.4
[SiW <sub>12</sub> O <sub>40</sub> ] <sup>4-</sup> (SiK <sup>4-</sup> )	99.8	-777	-1153	12.9
[AlW <sub>12</sub> O <sub>40</sub> ] <sup>5-</sup> (AlK <sup>5-</sup> )	97.2	-1049	-1543	18.7
[ZnW <sub>12</sub> O <sub>40</sub> ] <sup>6-</sup> (ZnK <sup>6-</sup> )	96.2	-1216	-1986	23.7

[a] The % *time binding* averaged over 100 ns of MD trajectories sampling data every 4 ps. Interaction energies,  $E_{\text{POM}\cdots\text{HEWL}}$  and  $E_{\text{POM}\cdots\text{water}}$  in  $\text{kJ mol}^{-1}$ , obtained from 50 ns simulation in the absence of solvent or protein, respectively. Number of H-bonds in the first solvation shell derived from the same MD simulations of POMs in water.

Interestingly, there is no linear relationship between POM charge and protein affinity. Instead, we found a quadratic polynomial correlation ( $r^2 = 0.98$ ) in which the SiK<sup>4-</sup> anion, with an intermediate charge value of -4, shows the highest protein affinity (see Figure 3). Experimentally, the higher POM charge had been correlated to larger binding affinity in the inhibition of amyloid  $\beta$  peptides,<sup>[19]</sup> and the selective precipitation of prions by the POM complexes.<sup>[26]</sup> This apparent charge-affinity relationship would only explain the increasing domain of the equation reported in Figure 3. On the other hand, an inverse correlation was found between the negative charge of a series of Keggin-type anions with charges ranging from -4 to -6 and their capacity to inhibit the diphenolase activity of mushroom tyrosinase *abPPO4*.<sup>[28]c</sup> Thus, we suspect that the analyzed datasets covered only a narrow range of charges within the same POM size, providing a partial description of the effect. In fact, analysis of the interaction between charged ligands and proteins had revealed that binding energy has a quadratic form on the charges of the ligand.<sup>[37],[38]</sup> This complex picture was attributed to the delicate balance between two effects of opposite sign: protein-ligand electrostatic interaction and ligand desolvation incurred upon binding. Thus, too weak electrostatic protein-ligand interaction as well as too strong ligand-solvent interaction in the unbound state result in a sub-optimal binding. According to the quantitative model built by Sulea and Purisima, the intermolecular Coulomb interaction energy increases linearly with the charge while the desolvation energy upon binding has a parabolic form.<sup>[38]</sup> Moreover, for the analogous, chaotropic borane anions a quadratic relationship was observed between

the binding affinity to estrogen receptor and their hydrophobicity,<sup>[39]</sup> which can be viewed as the inverse of the charge. The effects governing these non-linear correlations are very intricate at the level of accurate molecular understanding and qualitative predictions; and their atomistic description is still lacking.

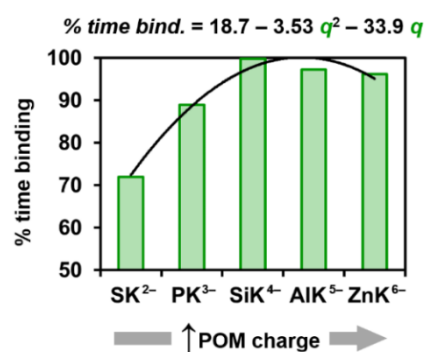


**Figure 3.** Protein affinity, measured as percentage of simulated time in which POM interacts with HEWL protein (% *time binding*), as function of the POM charge in [X<sup>n</sup>W<sub>12</sub>O<sub>40</sub>]<sup>(6-n)-</sup>. The relationship was fitted to a quadratic polynomial regression model ( $r^2 = 0.98$ ): solid black curve and equation on the top.

Figures 4 and 5 and values of Table 1 (columns 3rd – 5th) collect the results of further analysis of POM interactions with the protein and with water solvent as a function of the anion charge. As Figure 4 shows, the POM $\cdots$ water interaction energy in the absence of the protein follows a quadratic growth with the POM charge, while the POM $\cdots$ protein interaction increases linearly if solvent effects are neglected, in agreement with the electrostatic model proposed by Sulea and Purisima.<sup>[38]</sup> Thus, the two competing interactions increase with the POM charge at different rates explaining why the POM affinity reaches a maximum at intermediate charge values.

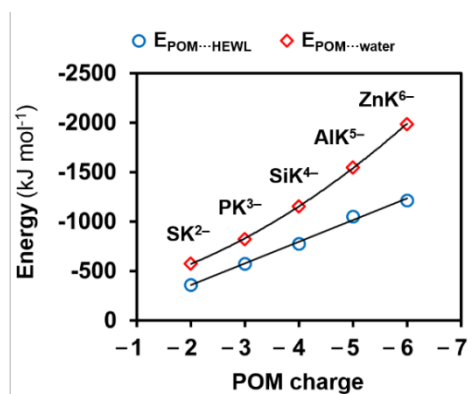


**Figure 4.** Average POM $\cdots$ HEWL (blue circles) and POM $\cdots$ water (red diamonds) interaction energies (in  $\text{kJ mol}^{-1}$ ) for the differently charged Keggin-type anions. Simulations performed in the absence of solvent and of protein, respectively. The  $E_{\text{POM}\cdots\text{HEWL}}$  and  $E_{\text{POM}\cdots\text{water}}$  on the POM charge were fitted, respectively, to linear ( $r^2 = 0.996$ ) and to a quadratic polynomial ( $r^2 = 0.999$ ) regression models.

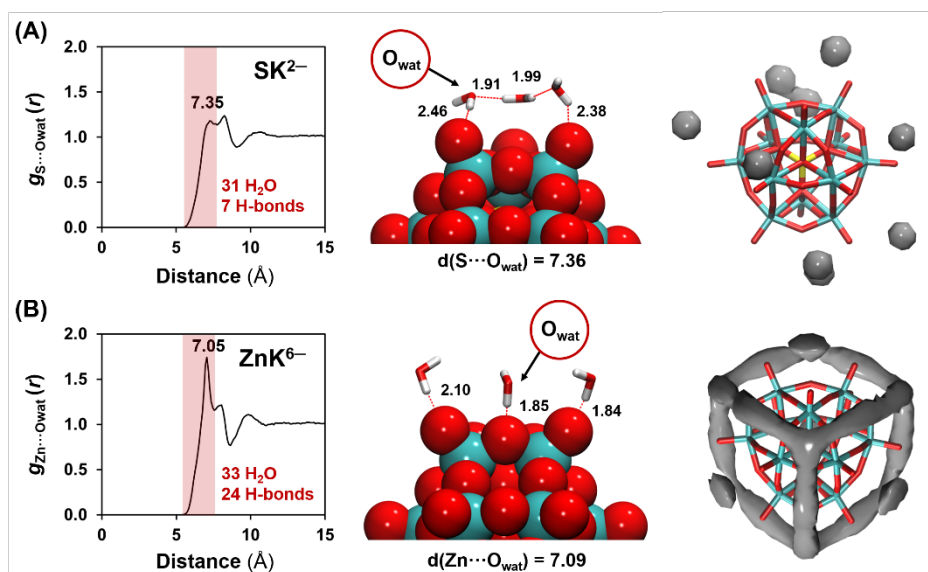


**Figure 5.** Radial distribution function (RDF) between the POM centre of mass and the oxygen atom of water molecules for  $\text{SK}^{2-}$  (A) and  $\text{ZnK}^{6-}$  (B) averaged over the last 20 ns of a 50 ns simulation carried out in the absence of protein. Each RDF is accompanied by a representative snapshot of the water distribution around each POM and a representation of the volumetric density of water molecules gathered in the first peak of each RDF.

To explain the counterintuitive non-linear relationship of the  $E_{\text{POM}\cdots\text{water}}$  with the POM charge, we analyzed the solvation shells around the POM and the variation of hydrogen bonding patterns, which have been used to understand the difference between chaotropic (water-structure-breaking) and kosmotropic (water-structure-forming) properties of ions.<sup>[17],[40],[41]</sup> Figure 5 compares the POM $\cdots$ water radial distribution functions (RDFs) for the two extreme charge cases  $\text{SK}^{2-}$  and  $\text{ZnK}^{6-}$  (see Figure S3 for the other Keggin anions). In going from  $\text{SK}^{2-}$  to  $\text{ZnK}^{6-}$ , there is an appreciable sharpening of the first RDF peak, similar to that observed for a series of polyoxovanadates with different charge.<sup>[42]</sup> Interestingly, for both POMs the first peak integrates to a similar number of water molecules per anion unit (31 for  $\text{SK}^{2-}$  vs 33 for  $\text{ZnK}^{6-}$ ), but the average number of anion-water hydrogen bonds increases dramatically, from 7.3 in  $\text{SK}^{2-}$  to 23.7 in  $\text{ZnK}^{6-}$  (see Table 1 and Figure 5). Figure 5 also shows typical snapshots illustrative of the difference in hydrogen bonding patterns. In  $\text{ZnK}^{6-}$ , the first solvation shell of water molecules is more structured and the bridging oxygen of the POM participate more actively in the hydrogen bonding network (Figure 5 and S4). The more organized water structure in  $\text{ZnK}^{6-}$  is reflected in the volumetric density of water molecules surrounding each POM (Figure 5).

The first consequence of the change in hydrogen bonding pattern is that upon increasing the negative charge of the POMs, the strength and the number of hydrogen bonds with water solvent increase, leading to a quadratic growth of the  $E_{\text{POM}\cdots\text{water}}$  interaction energy. Moreover, longer residence of the hydrogen bonds and more localized waters in  $\text{ZnK}^{6-}$  (Figure 5) can be related to slower water dynamics over the anion surface.<sup>[43]</sup> Therefore, less chaotropic (more kosmotropic) properties are expected for highly charged POMs resulting in proportionally larger desolvation energies, and consequently in less affinity towards proteins. On the other hand, for moderately charged POMs the first solvation shell is less structured and diffuses faster, resulting in lower desolvation energies. Overall, to

enhance POM affinity towards proteins, one needs to balance the strength of POM $\cdots$ protein and POM $\cdots$ water interactions. For HEWL, this situation is found for the moderately charged  $\text{SiK}^{4-}$  anion, but depending on the topology of the biological system, the optimal POM charge might be shifted. These results are highly correlated with very recent observation by Rompel et al. that identified moderately charged  $[\text{SiW}_{12}\text{O}_{40}]^{4-}$  anion as the most pronounced inhibitor of mushroom tyrosinase *ab*PP04, while for higher charged Keggin structures the inhibitory capacity decreases.<sup>[28]</sup>

#### Influence of the POM size and shape.

Next, we varied systematically the size and shape of the POM keeping constant its charge density, using the charge per metal ratio ( $q/M$ ) as a magnitude that correlates with the charge density.<sup>[30],[36]</sup> The selected structures with  $q/M = 0.33$  are shown in Figure 1 and comprise: the  $[\text{W}_6\text{O}_{19}]^{2-}$  Lindqvist anion ( $\text{L}^{2-}$ ), the  $[\text{SiW}_{12}\text{O}_{40}]^{4-}$  Keggin anion ( $\text{SiK}^{4-}$ ), the  $[\text{P}_2\text{W}_{18}\text{O}_{62}]^{6-}$  Wells–Dawson anion ( $\text{WD}^{6-}$ ), and the  $[\text{HThP}_5\text{W}_{30}\text{O}_{110}]^{10-}$  Preyssler-like anion, ( $\text{HThP}^{10-}$ ). Note that the  $\text{HThP}^{10-}$  anion corresponds to a model structure in which one internal oxygen atom was protonated in order to ensure the same  $q/M$  ratio along the series. Moreover, the volume ratio  $V_{\text{POM}}/V_{\text{total}}$  was kept approximately constant, by adjusting the dimension of the simulated system (see Figure S5) in order to avoid the bias of the density of POM on POM $\cdots$ protein contacts (9.45 - 9.52 g L $^{-1}$  range). Also, we performed these simulations keeping constant the molality of POM and protein species (see Table S1), and the obtained results are consistent with the qualitative trends defined by the simulations with constant  $V_{\text{POM}}/V_{\text{total}}$  ratio, described hereunder.

Table 2 (second column) collects the values of the % *time binding* for the series of POMs with different sizes, computed from simulations with the same density of POM. All the anions display a high affinity to the protein, indicating that the  $q/M$  ratio of 0.33 corresponds to the *optimal* charge density to interact with

HEWL. Among the series, the smallest  $L^{2-}$  anion presents a less persistent interaction and it moves over the protein surface and in/out of the solution. Contrastingly, the other anions ( $SiK^{4-}$ ,  $WD^{6-}$ , and  $HThP^{10-}$ ) interact persistently at a single cationic site at each MD run (see Figure S6). The sub-optimal interaction of  $L^{2-}$  can be ascribed to the fact that its size cannot interact with several amino acids simultaneously resulting in less efficient contacts with the protein than bigger anions.<sup>[30]</sup> The average values of anion-solvent interactions normalized by the number of solvent-accessible atoms have very similar values confirming that the differences in the protein affinity are due to the influence of the size, not biased by electrostatics (see Table 2, fourth column). There are several experiments that could be directly related to our findings for Lindqvist anion. For example, Parac-Vogt et al. reported that Lindqvist anions were less active than bigger structures in the hydrolysis of proteins.<sup>[13],[14]</sup> Moreover, spectroscopic studies revealed that among several POMs with different structures, the smallest Lindqvist structure was found to be the one influencing the least the structure of the protein.<sup>[15]</sup>

**Table 2.** Comparison of the HEWL affinity and protein and solvent interaction of  $L^{2-}$ ,  $SiK^{4-}$ ,  $WD^{6-}$ , and  $HThP^{10-}$  POMs having different size and shape and the same charge density ( $q/M = 0.33$ ).<sup>[a]</sup>

anion	% time binding	$E_{POM \cdots HEWL}$	$E_{POM \cdots water/atom}$	$E_{desolv}$
$[W_6O_{19}]^{2-}$ ( $L^{2-}$ )	94.2	-152	-34	+172
$[SiW_{12}O_{40}]^{4-}$ ( $SiK^{4-}$ )	99.8	-239	-32	+265
$[P_2W_{18}O_{62}]^{6-}$ ( $WD^{6-}$ )	99.4	-261	-32	+264
$[HThP_5W_{30}O_{110}]^{10-}$ ( $HThP^{10-}$ )	99.0	-325	-32	+267

[a] Interaction energies in  $\text{kJ mol}^{-1}$ .  $E_{POM \cdots water/atom}$  corresponds to the interaction energy with water normalized per solvent-accessible atom, and  $E_{desolv}$  accounts for the loss of  $E_{POM \cdots water}$  in going from the unbound to the bound situation. Data were sampled every 4 ps from the 100 ns MD trajectories.

The evolution of protein affinity with the size is similar to that found with charge density, that is, it increases until a maximum (Keggin structure) and then decreases less steeply (Table 2). Note however that in this case the dataset is not large enough to set a reliable quantitative relationship. To understand the origin of the observed time-dependence we analyzed separately the interaction of the POMs with the solvent and the protein as a function of the size. Figure 6 shows that the  $POM \cdots water$  interaction energy ( $E_{POM \cdots water}$ ) increases linearly with the number of addenda W atoms, because so does the number of solvent-accessible atoms, which support similar atomic charges. Differently, the  $POM \cdots protein$  interaction energy ( $E_{POM \cdots HEWL}$ ) grows logarithmically with the cluster size (see Figure 6). A closer look to the interaction mode of large anions revealed that the *non-spherical* Wells–Dawson ( $WD^{6-}$ ) and Preyssler ( $HThP^{10-}$ ) anions do not interact with HEWL using the largest possible surface area but they do it in an edgewise manner

through their narrowest side (see Figure 7 for representative snapshots of these interactions). Moreover, the computed volumetric density of  $POM \cdots protein$  contacts for  $WD^{6-}$  and  $HThP^{10-}$  species confirms these interaction modes (Figure S7). Accordingly, the computed POM desolvation energies upon binding to HEWL ( $E_{desolv}$ ) are similar for  $SiK^{4-}$ ,  $WD^{6-}$  and  $HThP^{10-}$  anions (see Table 2 and Table S2 for details). Thus, one can say that Wells–Dawson type  $WD^{6-}$  and Preyssler-type  $HThP^{10-}$  anions interact with HEWL in a *Keggin-like* manner, and therefore, not only POM size but also the shape is important to understand their interaction with biomolecules.

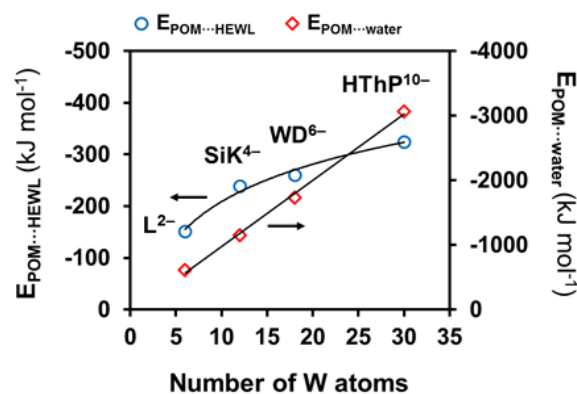


**Figure 6.** Average  $POM \cdots HEWL$  (blue circles) and  $POM \cdots water$  (red diamonds) interaction energies (in  $\text{kJ mol}^{-1}$ ) as a function of the number of W atoms in  $L^{2-}$ ,  $SiK^{4-}$ ,  $WD^{6-}$  and  $HThP^{10-}$  anions.  $E_{POM \cdots HEWL}$  averaged for snapshots with  $POM \cdots HEWL$  distance  $\leq 3.5$  Å.  $E_{POM \cdots water}$  averaged from 20ns simulations in the absence of protein and fitted to a linear regression model ( $r^2 = 0.99$ ).

The origin of this *Keggin-like* interaction mode in larger anions with non-spherical shape may be related to the non-homogeneous charge distribution. Electrostatic repulsion within the POM causes the charge density to be higher at the most peripheral parts, accumulating larger negative charge at the most distal oxygen atoms (see Figure S8). Thus, these oxygen centers are expected to interact strongly with the protein. Conversely, we evaluate the importance of the size of cationic pockets at the HEWL protein by comparing simulations of  $WD^{6-}$  anion with new ones of the same Wells–Dawson structure setting all the atomic charges to zero,  $WD^0$ . The computed volumetric densities of the  $POM \cdots protein$  contacts reveal that both species interact with HEWL protein through the same cap region (see Figure S9) indicating that charge distribution within the POM does not rule the directionality of the interaction but the intensity. Finally, one should consider that for POMs bigger than Keggin structure ( $WD^{6-}$  and  $HThP^{10-}$ ) the POM surface exposed to the solvent enlarges  $POM \cdots water$  interactions. This increases the forces that pull the POMs towards the solvent bulk counterbalancing  $POM \cdots protein$  interactions and explaining the smooth decrease in the % time binding (see Table 2). Overall these results indicate that in solution cationic pockets in HEWL are size-specific for Keggin-sized POMs (of about 1 nm of side length) determining the optimal size for POM affinity.

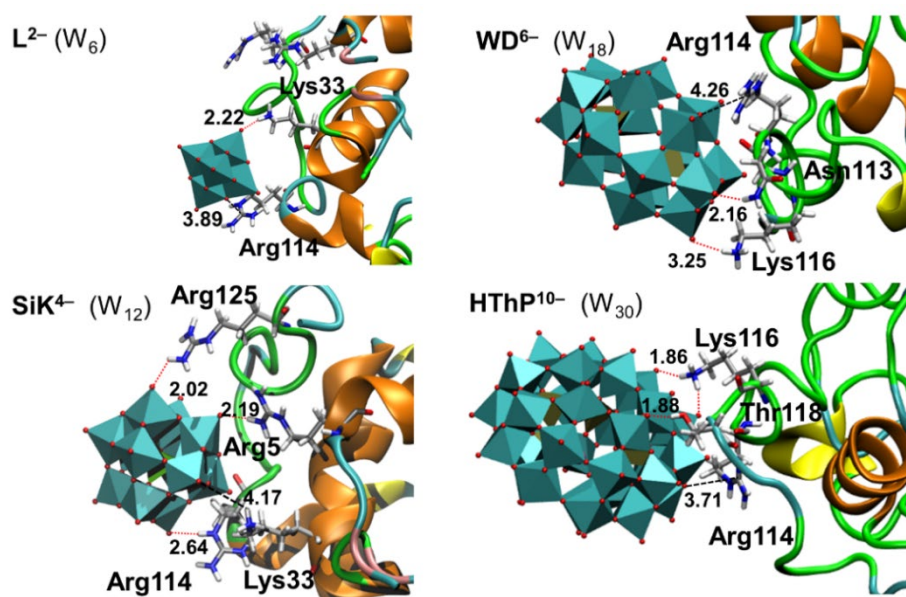


Figure 7. Representative snapshots of the interaction between HEWL and four POMs with the same charge density ( $q/M$ ) but different structure.

#### Development of a multidimensional model.

After analyzing the influence of different POM features separately, we sought to build a multidimensional mathematical model correlating protein affinity of POMs with their charge density and molecular size and shape. The dataset comprises previous simulated structures and five additional ones, including model systems, selected to balance the chemical space. Thus, we performed analogous simulations of HEWL protein in solution with the following five structures: the one electron-oxidized Lindqvist anion [ $W_6O_{19}$ ]<sup>3-</sup> (**L<sup>3-</sup>**), the one electron-reduced anion [ $W_6O_{19}$ ]<sup>3-</sup> (**L<sup>3-</sup>**), the tungstosulfate [ $S_2W_{18}O_{62}$ ]<sup>4-</sup> (**SWD<sup>4-</sup>**) and tungstosilicate [ $Si_2W_{18}O_{62}$ ]<sup>3-</sup> (**SiWD<sup>3-</sup>**) with Wells–Dawson structure and the classical sodium-containing Preyssler anion [ $NaP_5W_{30}O_{110}$ ]<sup>14-</sup> (**NaP<sup>14-</sup>**). For each set of simulations, we evaluated the % *time binding* as a response variable associated to protein affinity. To describe the electrostatic features of the POMs we used the charge per metal ratio ( $q/M$ ) as numerical parameter to account for the charge density of the anions. As discussed above both the size and the shape have an influence on protein affinity. To describe simultaneously both geometric features we propose a novel descriptor, the shape-weighted volume ( $V_s$ ). The  $V_s$  is calculated according to equation 1, where  $n_w$  is the number of addenda ions ( $W$ ) and  $r_{max}$  represents the maximum side length in the POM structure in nm (see Figure 8 for a graphical description and Table S3 for numerical values). Table 3 collects the values of the response variable (% *time binding*) and the descriptors ( $q/M$  and  $V_s$ ) for the 13 structures of the dataset ordered in increasing values of the response variable.

The calculated % *time binding* is correlated to the descriptors  $q/M$  and  $V_s$ , and their second-order terms ( $q/M^2$  and  $V_s^2$ ), which account for quadratic dependence found above. Using partial least square (PLS) regression technique and the descriptors normalized to the highest values, we obtain a predictive model in which full leave-one-out (LOO) cross-validation leads to a value of  $r^2$  for the fitting of 0.97 and a predictive ability  $q^2$  of 0.88 with three PLS. In quantitative structure-activity relationship

(QSAR) modelling, a model is considered to be predictive when the value of  $q^2$  is higher than 0.5, which is halfway between perfect prediction (1.0) and no model at all (0.0). Figure 9 shows the measured affinities plotted against the fitted values and the multidimensional QSAR equation. To further evaluate the prediction ability of our model, the dataset is divided into test (3 POMs of different protein affinity class) and training subsets (10 POMs) to develop an externally validated QSAR model. New QSAR models are generated with the training subsets and predictions were made for the test subsets (see Table S4 for details). We repeated the procedure 5 times obtaining good predictive models for the training set in all cases ( $q^2$  ranging from 0.78 to 0.92). From the 15 externally validated samples, 8 are excellently predicted with errors < 2 %, and average error ranges from 2.1 to 4.9%. The poorest predictions are obtained for **L<sup>2-</sup>** (7.6 %) **SK<sup>2-</sup>** (6.0 %) and **ZnK<sup>6-</sup>** (5.9 %), which correspond to species with structural features close to the limits of the analyzed chemical space. However, the overall validation supports the reliability of the QSAR model and quantitative (or semi-quantitative) ability to predict the affinity of POMs to HEWL proteins.

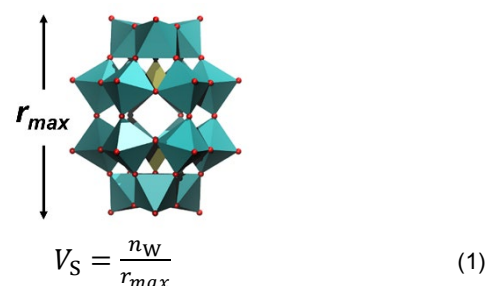


Figure 8. Graphical representation of the  $r_{max}$  parameter used to calculate the shape-weighted Volume ( $V_s$ ) molecular descriptor.

**Table 3.** Classification of the simulated systems as a function of the % time binding, and values of molecular descriptors charge density ( $q/M$ ) and shape-weighted volume ( $V_s$ ).

classification	POM	$q/M$	$V_s$	% time binding <sup>[a]</sup>
Moderate interaction (< 90 %)	$L^-$	0.17	6.8	69.7
	$SK^{2-}$	0.17	11.4	72.0
	$L^{3-}$	0.50	6.8	86.0
	$SWD^{4-}$	0.22	11.7	87.0
	$PK^{3-}$	0.25	11.4	88.9
Strong interaction (90–98 %)	$L^{2-}$	0.33	6.8	94.2
	$ZnK^{6-}$	0.50	11.4	96.2
	$AlK^{5-}$	0.42	11.4	97.2
	$SiWD^{6-}$	0.44	11.7	97.8
Persistent interaction (98–100 %)	$NaP^{14-}$	0.47	16.6	98.9
	$HTHP^{10-}$	0.33	16.6	99.0
	$WD^{6-}$	0.33	11.7	99.4
	$SiK^{4-}$	0.33	11.4	99.8

[a] Values are sampled every 4 ps from the 100 ns MD trajectories.

$$\% \text{ time bind.} = -6.8 - 135.1 \frac{q}{M^2} + 210.2 \frac{q}{M} - 35.5 V_s^2 + 61.7 V_s$$

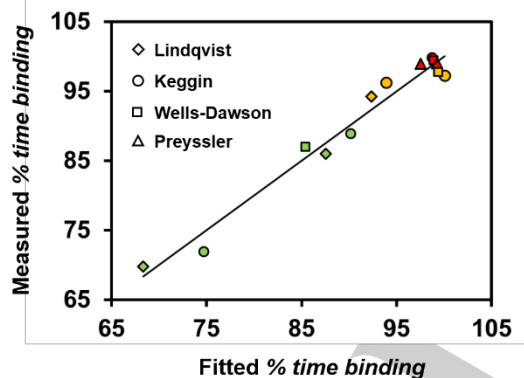


**Figure 9.** Measured versus fitted % time binding for the 13 POMs species using a linear regression model with  $q/M$ ,  $V_s$ ,  $q/M^2$  and  $V_s^2$  normalized descriptors, and the resulting QSAR equation. Diamonds, circles, squares and triangles correspond to Lindqvist, Keggin, Wells-Dawson and Preyssler structures, respectively. Green for moderate, yellow for strong and red for persistent interactions.

The use of normalized, chemically-meaningful descriptors allows to extract some (bio)chemical information from the QSAR equation depicted in Figure 9. Both the charge density and the geometry of the POM have a non-linear correlation with protein affinity. The significant weight of second-order terms indicates that protein affinity has a quadratic-like dependence of both properties. This is the result of a delicate balance between POM⋯protein and POM⋯solvent interactions. Moreover, the higher absolute values of the  $q/M$  coefficients compared to those  $V_s$  indicate that the protein affinity is mainly governed by the

charge density of the polyoxoanion and it is less affected by its bulkiness or its shape. Table S5 compiles the values of the normalized descriptors and the QSAR equation with non-normalized coefficients can be found in the Supporting Information. Finally, Figure 10 shows the response surface predicted by the QSAR model as function of the POM molecular descriptors. Within the analyzed chemical space, the map allows identifying a region (dark red) in which the POM⋯protein interactions are maximized. We also note that the multidimensional model must be interpreted qualitatively, as a mathematical equation which points out the trends and the weight of the different factors influencing POM affinity.

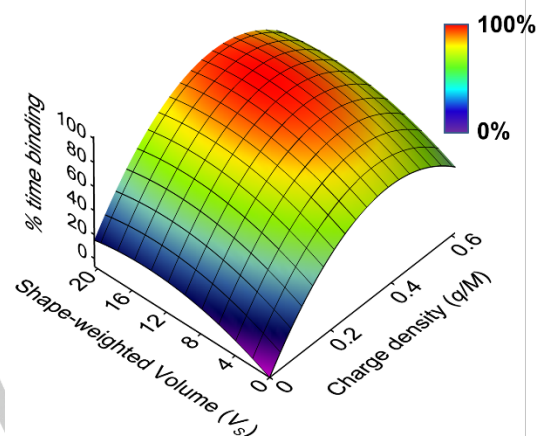


**Figure 10.** Three-dimensional response surface of the K as function of the charge density ( $q/M$ ) and the shape-weighted volume ( $V_s$ ) descriptors of the POMs using QSAR model. Red regions represent the most persistent interactions, and thus, the highest protein affinities.

## Conclusion

A systematic Molecular Dynamics (MD) study allowed setting structure–activity relationships between the molecular composition of chaotropic polyoxometalate (POM) anions and their affinity to biomolecules, using hen egg-white lysozyme (HEWL) as a model protein. When the charge of the POM is varied systematically keeping the same size and shape ( $[X^{n+}W_{12}O_{40}]^{(8-n)-}$ ;  $X^{n+} = S^{VI}, P^V, Si^{IV}, Al^{III}$  and  $Zn^{II}$ ), the protein affinity shows a quadratic dependence with a maximum at charge 4− ( $X = Si^{IV}$ ,  $q/M = 0.33$ ). The effects governing this non-linear correlation are very intricate and depend on the delicate balance between the POM⋯protein and the POM⋯water interactions. While the POM⋯protein interaction energy increases linearly with the POM charge, the POM⋯water interaction showed a parabolic growth. Highly charged POM anions have less chaotropic (more kosmotropic) character that results in a more structured solvation shell of water molecules, in which the strength and number of hydrogen bonds increases. This accurate atomistic description of the change in hydrogen bonding pattern revealed that POMs with high charge densities have proportionally larger desolvation energies, and consequently, less affinity towards proteins. When the size and shape of the POM is varied keeping its charge density (number of  $W = 6, 12, 18$  and  $30$ ;  $q/M = 0.33$ ), simulations indicate that the interactions of POM with proteins are size-specific, being the size of Keggin-type anion (~1 nm length;  $W = 12$ ) optimal for fitting into the cationic pockets of HEWL. Smaller structures such

as the Lindqvist ( $W = 6$ ) have sub-optimal interaction with the protein because they cannot interact with several amino acids simultaneously. Shape is also important since larger non-spherical anions such as the Wells-Dawson ( $W = 18$ ) and the Preyssler ( $W = 30$ ) interact in an edgewise (*Keggin-like*) manner exposing a large part of their oxide surface to the solvent, which pulls the POMs towards the bulk.

Finally, we were able to build a multidimensional model with predicting ability ( $r^2 = 0.97$  and  $q^2 = 0.88$ ) that correlates quantitatively the protein affinity expressed as the % *time binding* and two handy molecular descriptors related to the charge density of the POM (charge per metal atom ratio;  $q/M$ ) and to its size and shape (shape-weighted volume;  $V_s$ ). The QSAR model indicates that the charge density of POMs influences their affinity to proteins in a larger extent than their molecular size and shape. Furthermore, this study evinces the capability of atomistic simulations to set structure–affinity relationships for the binding of inorganic clusters such as POMs to biological systems using time–derived variables.

## Computational Details

Classical MD simulations were carried out using GROMACS 4.5.4 software<sup>[44]</sup> and the AMBER 99 force field,<sup>[45]</sup> which has been successfully employed in a previous work to model POM–protein interactions.<sup>[30]</sup> The potential energy  $U$  of the system is empirically described by the sum of the bond, the angle, and the dihedral deformation energies and the pair-wise additive 1–6–12 (electrostatic and van der Waals) interactions between non bonded atoms. Parameters for the topology of the different polyoxoanions were obtained following the procedure of Bonet-Avalos, Bo, Poblet et al.<sup>[46]</sup> CHelpG atomic charges were obtained with the Gaussian09 package<sup>[47]</sup> at the DFT level (BP86 functional)<sup>[48]</sup> using the LANL2DZ basis set.<sup>[49]</sup> Geometry optimizations were performed with solvent effects of water using the IEF-PCM model<sup>[50]</sup> as implemented in Gaussian09 package<sup>[47]</sup>. Lennard–Jones parameters for W and O atoms of the POMs were taken from previous works,<sup>[30],[46],[51]</sup> and those for Al<sup>III</sup>, Si<sup>IV</sup> and Th<sup>IV</sup> were taken from the UFF force field.<sup>[52]</sup> The geometry of the 8+ charged HEWL protein was taken from the protein data bank (PDB) database (PDB ID: 3IJV).<sup>[53]</sup>

For the MD simulations, a cubic simulation box was built around the protein, which was filled by water molecules. One POM was inserted randomly in each simulation box, and the initial POM position was kept for all the runs. The box size was set to keep the same  $V_{\text{POM}}/V_{\text{total}}$  in all the simulations and roughly, the density of POM ( $\rho_{\text{POM}}/L_{\text{water}}^{-1}$ ). In particular, when simulating POMs of different sizes, it is of great importance to maintain the same volume ratio in order to avoid overestimations in quantifying the interaction of bulkier POMs or underestimate it for smaller ones. Cl<sup>−</sup> or Na<sup>+</sup> counter ions were added to neutralize the system. Detailed information of each simulated system can be found in Table S6. Additionally, simulations with POMs of different sizes were also performed keeping constant the same number of water molecules and in turn, the molal concentration of POM and protein (see Table S1). Water was represented with the TIP3P model.<sup>[54]</sup> All simulations were performed with 3D–periodic boundary conditions using an atom cutoff of 14 Å for van der Waals and of 10 Å for Coulombic interactions between atoms separated by more than 3 bonds. Long–range electrostatic interactions were corrected by using the particle–particle mesh Ewald (PME) summation method.<sup>[55]</sup> The simulations were performed at 300 K starting with random velocities. The temperature was controlled by coupling the system to a thermal bath using the Berendsen algorithm<sup>[56]</sup> with a relaxation time of 0.1 ps to perform the simulations within an NVT ensemble. In simulations done under an isothermal–isobaric (NPT) regime, the system was also coupled to a barostat using

the Berendsen algorithm<sup>[56]</sup> with a relaxation time of 0.1 ps. Newton equations of motion were integrated using the leap–frog algorithm,<sup>[57]</sup> and a time step of 1 fs. The bonds involving H atoms were restrained using the LINCS algorithm.<sup>[58]</sup>

Before the production runs, all the systems were equilibrated by 1000 steps of energy minimization followed by a 250 ps simulation fixing the solute molecules in order to relax the solvent around them. Then, a 250 ps at constant volume (NVT) with the solvent relaxed, a 500 ps simulation at constant temperature (300 K) and pressure (1 atm) to stabilize the pressure and thus the density and a last 250 ps simulation (NVT). Finally, five independent runs of 20 ns dynamics were performed at constant volume and at 300 K for each system. For the sake of comparison, some NVT simulations were repeated using the velocity rescaling algorithm<sup>[59]</sup> and found that results do not vary significantly. Recently, this molecular dynamics protocol have been successfully employed to study aggregation processes of POMs in solution obtaining results consistent with experiments.<sup>[42],[60]</sup> The time evolution of the average values of the % *time binding* was statistically analysed (see Figure S11 and Table S6 in Supporting Information) indicating that this time average property converges after 100 ns providing a reliable and precise sampling for POM–protein interactions.

Main characteristics of the additional simulations used to build the multivariate model are displayed in Table S7 and Table S8 collects the features of the simulations used to evaluate the POM–protein and POM–water interaction energies in the absence of solvent and protein, respectively. For the multivariate model (Table S7), every POM structure was analyzed following the same protocol described above, while to determine individual interaction energies (Table S8), one single run of 50 ns was performed for each POM.

## Acknowledgements

This work was supported by the Spanish Ministry of Economy and Competitiveness (Projects CTQ2017-87269-P and PGC2018-100780-B-I00) and the Generalitat de Catalunya (2017-SGR629). J.M.P thanks the ICREA foundation for an ICREA ACADEMIA award.

**Keywords:** structure-activity relationships • chaotropic anions • polyoxometalates • protein interaction • molecular dynamics

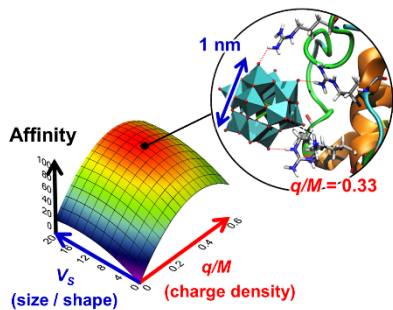
- [1] M. T. Pope, *Heteropoly and isopoly oxometalates*, Springer–Verlag, New York, 1983.
- [2] D. L. Long, R. Tsunashima, L. Cronin, *Angew. Chem., Int. Ed.* **2010**, *49*, 1736–1758; b) A. Proust, R. Thouvenot, P. Gouzerh, *Chem. Commun.* **2008**, 1837–1852; c) N. Mizuno, K. Yamaguchi, *Chem. Rec.* **2006**, *6*, 12–22.
- [3] For some reviews, see: a) A. Proust, B. Matt, R. Villanneau, G. Guillemot, P. Gouzerh, G. Izzet, *Chem. Rev.* **2012**, *41*, 7605–7622; b) Y. F. Song, R. Tsunashima, *Chem. Rev.* **2012**, *41*, 7384–7402; c) Y. Wang, I. Weinstock, *Chem. Rev.* **2012**, *41*, 7479–7496.
- [4] For some reviews, see: a) S. S. Wang, G. Y. Yang, *Chem. Rev.* **2015**, *115*, 4893–4962; b) H. Lv, Y. V. Geletii, C. Zhao, J. W. Vickers, G. Zhu, Z. Luo, J. Song, T. Lian, D. G. Musaev, C. L. Hill, *Chem. Soc. Rev.* **2012**, *41*, 7572–7589.
- [5] For some reviews, see: a) H. Stephan, M. Kubeil, F. Emmerling, C. E. Muller, *Eur. J. Inorg. Chem.* **2013**, 1585–1594; b) M. Aureliano, G. Franqueza, C. A. Ohlin, *Dalton Trans.* **2013**, *42*, 11770–11777; c) J. T. Rhule, C. L. Hill, D. A. Judd, *Chem. Rev.* **1998**, *98*, 327–358.
- [6] K. Tomita, T. Yamase, K. Shishido, *Inorg. Chim. Acta.* **1989**, *157*, 167–169; b) T. Yamase, *J. Mater. Chem.* **2005**, *15*, 4773–4782; c) S. Mitsui, A. Ogata, H. Yanagie, H. Kasano, T. Hisa, T. Yamase, M. Eriguchi, *Biomed. Pharmacother.* **2006**, *60*, 353–358.

- [7] K. Narasimhan, S. Pillay, N. R. B. Ahmad, Z. Bikadi, E. Hazai, L. Yan, P. R. Kolatkar, K. Pervushin, R. Jauch, *ACS Chem. Biol.* **2011**, *6*, 573–581.
- [8] F. Pu, E. Wang, H. Jiang, J. Ren, *Mol. BioSyst.* **2013**, *9*, 113–120.
- [9] A. Bijelic, A. Rompel, *Coord. Chem. Rev.* **2015**, *299*, 22–38.
- [10] J. Thygesen, S. Weinstein, F. Franceschi, A. Yonath, *A. Structure* **1996**, *4*, 513–518; b) A. Bashan, A. Yonath, *J. Mol. Struct.* **2008**, *890*, 289–294; c) D. Janell, A. Tocilj, I. Kölln, F. Schlünzen, M. Glühmann, H. A. S. Hansen, J. Harms, A. Bahan, I. Agmon, H. Bartels, M. Kessler, S. Weinstein, F. Franceschi, A. Yonath, A. in *Polyoxometalate Chemistry*, Pope M. T. and Müller, A. Eds., 2001, 391–415, Kluwer Academic Publishers.
- [11] T. L. H. Giang, G. Absillis, S. R. Bajpe, J. A. Martens, T. N. Parac-Vogt, *Eur. J. Inorg. Chem.* **2013**, 4601–4611; b) T. L. H. Giang, G. Absillis, T. N. Parac-Vogt, *Dalton Trans.* **2013**, *42*, 10929–10938; c) G. Absillis, T. N. Parac-Vogt, *Inorg. Chem.* **2012**, *51*, 9902–9910; d) S. Vanhaecht, G. Absillis, T. N. Parac-Vogt, *Dalton Trans.* **2012**, *41*, 10028–10034.
- [12] K. Stroobants, E. Moelants, H. G. T. Ly, P. Proost, K. Bartik, T. N. Parac-Vogt, *Chem. Eur. J.* **2013**, *19*, 2848–2858; b) K. Stroobants, V. Goovaerts, G. Absillis, G. Bruylants, E. Moelants, P. Proost, T. N. Parac-Vogt, *Chem. Eur. J.* **2014**, *20*, 9567–9577.
- [13] K. Stroobants, G. Absillis, E. Moelants, P. Proost, T. N. Parac-Vogt, *Chem. Eur. J.* **2014**, *20*, 3894–3897.
- [14] H. G. T. Ly, G. Absillis, R. Janssens, P. Proost, T. N. Parac-Vogt, *Angew. Chem. Int. Ed.* **2015**, *54*, 7391–7394.
- [15] H. G. T. Ly, T. N. Parac-Vogt, *ChemPhysChem* **2017**, *18*, 2451–2458.
- [16] M. Arefian, M. Mirzaei, H. Eshtiagh-Hosseini, A. Frontera, *Dalton Trans.* **2017**, *46*, 6812–6829.
- [17] K. I. Assaf, W. M. Nau, *Angew. Chem. Int. Ed.* **2018**, *57*, 13968–13981.
- [18] G. Zhang, B. Keita, C. T. Craescu, S. Miron, P. de Oliveira, L. Nadjo, *J. Phys. Chem. B* **2007**, *111*, 11253–11259.
- [19] J. Geng, M. Li, J. Ren, E. Wang, X. Qu, *Angew. Chem. Int. Ed.* **2011**, *50*, 4184–4188.
- [20] S. Shigeta, S. Mori, J. Watanabe, M. Baba, A. M. Khenkin, C. L. Hill, R. F. Schinazi, *Antiviral Chem. Chemother.* **1995**, *6*, 114–122.
- [21] S. Shigeta, S. Mori, J. Watanabe, Y. Yamase, R. F. Schinazi, *Antiviral Chem. Chemother.* **1996**, *7*, 346–352.
- [22] T. Zhang, D. Fu, Y. Wu, Y. Wang, L. Wu, *Dalton Trans.* **2016**, *45*, 15457–15463.
- [23] R. Prudent, V. Mucadel, B. Laudet, C. Barette, L. Lafanechère, B. Hasenknopf, J. Li, S. Bareyt, E. Lacôte, S. Thorimbert, M. Malacria, P. Gouzerh, C. Cochet, *Chem. Biol.* **2008**, *15*, 683–692.
- [24] G. Zhang, B. Keita, C. T. Craescu, S. Miron, P. de Oliveira, L. Nadjo, *Biomacromolecules* **2008**, *9*, 812–817.
- [25] Y. Zhou, L. Zheng, F. Han, G. Zhang, Y. Ma, J. Yao, B. Keita, P. de Oliveira, L. Nadjo, *Colloids Surf. A* **2011**, *375*, 97–101.
- [26] I. S. Lee, J. R. Long, S. B. Prusiner, J. G. Safar, *J. Am. Chem. Soc.* **2005**, *127*, 13802–13803; b) H. Wille, M. Shanmugam, M. Murugesu, J. Ollesch, G. Stubbs, J. R. Long, J. G. Safar, S. B. Prusiner, *Proc. Natl. Acad. Sci. U.S.A.* **2009**, *106*, 3740–3745.
- [27] C. E. Müller, J. Iqbal, Y. Baqi, H. Zimmermann, A. Röllich, H. Stephan, *Bioorg. Med. Chem. Lett.* **2006**, *16*, 5943–5947; b) S.-Y. Lee, A. Fiene, W. Li, T. Hank, K. A. Brylev, V. E. Fedorov, J. Lecka, A. Haider, H.-J. Pietzsch, H. Zimmermann, J. Sévigny, U. Kortz, H. Stephan, C. E. Müller, *Biochem. Pharmacol.* **2015**, *93*, 171–181.
- [28] N. Gumerova, L. Krivosudský, G. Franqueza, J. Breibeck, E. Al-Sayed, E. Tanuhadi, A. Bijelic, J. Fuentes, M. Aureliano, A. Rompel, *Metallomics* **2018**, *10*, 287–295; b) A. Bijelic, M. Aureliano, A. Rompel, *Chem. Commun.* **2018**, *54*, 1153–1169; c) J. Breibeck, N. I. Gumerova, B. B. Boesen, M. Galanski, A. Rompel, *Sci. Rep.* **2019**, *9*, 5183.
- [29] C. Molitor, A. Bijelic, A. Rompel, *IUCrJ* **2017**, *4*, 734–740.
- [30] A. Solé-Daura, V. Goovaerts, K. Stroobants, G. Absillis, P. Jiménez-Lozano, J. M. Poblet, J. D. Hirst, T. N. Parac-Vogt, J. J. Carbó, *Chem. Eur. J.* **2016**, *22*, 15280–15289.
- [31] A. Sap, E. De Zitter, L. Van Meervelt, T. N. Parac-Vogt, *Chem. Eur. J.* **2015**, *21*, 11692–11695.
- [32] L. Vandebroek, L. Van Meervelt, T. N. Parac-Vogt, *Acta Crystallogr. C* **2018**, *74*, 1348–1354.
- [33] L. Vandebroek, E. De Zitter, H. G. T. Ly, D. Coniç, T. Mihaylov, A. Sap, P. Proost, K. Pierloot, L. Van Meervelt, T. N. Parac-Vogt, *Chem. Eur. J.* **2018**, *24*, 10099–10108; b) L. Vandebroek, Y. Mampaey, S. Antonyuk, L. Van Meervelt, T. N. Parac-Vogt, *Eur. J. Inorg. Chem.* **2019**, *3*, 506–511.
- [34] A. Bijelic, C. Molitor, S. G. Mauracher, R. Al-Oweini, U. Kortz, A. Rompel, *ChemBioChem* **2015**, *16*, 233–241.
- [35] T. J. Paul, T. N. Parac-Vogt, D. Quiñero, R. Prabhakar, *J. Phys. Chem. B* **2018**, *122*, 7219–7232; b) V. M. Jayasinghe-Arachchige, Q. Hu, G. Sharma, T. J. Paul, M. Lundberg, D. Quiñero, T. N. Parac-Vogt, R. Prabhakar, *J. Comp. Chem.* **2019**, *40*, 51–61.
- [36] X. López, J. J. Carbó, C. Bo, J. M. Poblet, *Chem. Soc. Rev.* **2012**, *41*, 7537–7571; b) X. López, P. Miró, J. J. Carbó, A. Rodríguez-Forteza, C. Bo, J. M. Poblet, *Theor. Chem. Acc.* **2011**, *128*, 393–404; c) X. López, J. A. Fernández, J. M. Poblet, *Dalton Trans.* **2006**, 1162–1167.
- [37] E. Kangas, B. Tidor, *J. Phys. Chem. B* **2001**, *105*, 880–888; b) L.-P. Lee, B. Tidor, *Nat. Struct. Biol.* **2001**, *8*, 73–76; c) L.-P. Lee, B. Tidor, *Protein Sci.* **2001**, *10*, 362–377.
- [38] T. Sulea, E. O. Purísima, *Biophys. J.* **2003**, *84*, 2883–2896; b) T. Sulea, E. O. Purísima, *J. Phys. Chem. B* **2001**, *105*, 889–899.
- [39] Y. Endo, K. Yamamoto, H. Kagechika, *Bioorg. Med. Chem. Lett.* **2003**, *13*, 4089–4092.
- [40] K. D. Collins, M. W. Q. Rev. *Biophys.* **1985**, *18*, 323–422.
- [41] Y. Marcus, *Chem. Rev.* **2009**, *109*, 1346–1370.
- [42] A. Solé-Daura, A. Notario-Estévez, J. J. Carbó, J. M. Poblet, C. de Graaf, K. Y. Monakhov, X. López, *Inorg. Chem.* **2019**, *58*, 3881–3894.
- [43] B. Sharma, A. Chandra, *J. Phys. Chem. B* **2018**, *122*, 2090–2101.
- [44] B. Hess, C. Kutzner, D. Van Der Spoel, E. Lindahl, *J. Chem. Theory Comput.* **2008**, *4*, 435–447; b) D. Van Der Spoel, E. Lindahl, B. Hess, G. Groenhof, A. E. Mark, H. J. C. Berendsen, *J. Comput. Chem.* **2005**, *26*, 1701–1718; c) H. J. C. Berendsen, D. Van Der Spoel, R. van Drunen, *Comput. Phys. Commun.* **1995**, *91*, 43–56.
- [45] J. M. Wang, P. Cieplak, P. A. Kollman, *J. Comput. Chem.* **2000**, *21*, 1049–1074.
- [46] F. Leroy, P. Miró, L. M. Poblet, C. Bo, J. B. Ávalos, *J. Phys. Chem. B* **2008**, *112*, 8591–8599; b) X. López, C. Nieto-Draghi, C. Bo, J. B. Ávalos, J. M. Poblet, *J. Phys. Chem. A* **2005**, *109*, 1216–1222.
- [47] Gaussian 09, Revision A.02, M. J. Frisch, G. W. Trucks, H. B. Schlegel, G. E. Scuseria, M. A. Robb, J. R. Cheeseman, G. Scalmani, V. Barone, G. A. Petersson, H. Nakatsuji, X. Li, M. Caricato, A. Marenich, J. Bloino, B. G. Janesko, R. Gomperts, B. Mennucci, H. P. Hratchian, J. V. Ortiz, A. F. Izmaylov, J. L. Sonnenberg, D. Williams-Young, F. Ding, F. Lipparini, F. Egidi, J. Goings, B. Peng, A. Petrone, T. Henderson, D. Ranasinghe, V. G. Zakrzewski, J. Gao, N. Rega, G. Zheng, W. Liang, M. Hada, M. Ehara, K. Toyota, R. Fukuda, J. Hasegawa, M. Ishida, T. Nakajima, Y. Honda, O. Kitao, H. Nakai, T. Vreven, K. Throssell, J. A. Montgomery, Jr., J. E. Peralta, F. Ogliaro, M. Bearpark, J. J. Heyd, E. Brothers, K. N. Kudin, V. N. Staroverov, T. Keith, R. Kobayashi, J. Normand, K. Raghavachari, A. Rendell, J. C. Burant, S. S. Iyengar, J. Tomasi, M. Cossi, J. M. Millam, M. Klene, C. Adamo, R. Cammi, J. W. Ochterski, R. L. Martin, K. Morokuma, O. Farkas, J. B. Foresman, and D. J. Fox, Gaussian, Inc., Wallingford CT, 2016.
- [48] A. D. Becke, *Phys. Rev. A* **1988**, *38*, 3098–3100; b) J. P. Perdew, *Phys. Rev. B* **1986**, *33*, 8822–8824.
- [49] P. J. Hay, W. R. Wadt, *J. Chem. Phys.* **1985**, *82*, 270–283.
- [50] E. Cancès, B. Mennucci, J. Tomasi, *J. Chem. Phys.* **1997**, *107*, 3032–3041.
- [51] P. Jiménez-Lozano, J. J. Carbó, A. Chaumont, J. M. Poblet, A. Rodríguez-Forteza, G. Wipff, *Inorg. Chem.* **2014**, *53*, 778.
- [52] A. K. Rappe, C. J. Casewit, K. S. Colwell, W. A. Goddard, W. M. J. Am. Chem. Soc. **1992**, *114*, 10024–10035.
- [53] E. Pechkova, S. K. Tripathi, C. Nicolini, Comparison of Lysozyme Crystals Grown by APA and Classical Hanging Drop Method, DOI: 10.2210/pdb2213ijv/pdb.
- [54] W. L. Jorgensen, J. Chandrasekhar, J. D. Madura, R. W. Impey, M. L. Klein, *J. Chem. Phys.* **1983**, *79*, 926–935.
- [55] T. Darden, D. York, L. Pedersen, *J. Chem. Phys.* **1993**, *98*, 10089–10092.

- [56] H. J. C. Berendsen, J. P. M. Postma, W. F. van Gunsteren, A. Di Nola, J. R. Haak, *J. Chem. Phys.* **1984**, *81*, 3684–3690.
- [57] R. W. Hockney, S. P. Goel, J. Eastwood, J. Quiet, *J. Comp. Phys.* **1974**, *14*, 148–158.
- [58] B. Hess, H. Bekker, H. J. C. Berendsen, J. G. E. M. Fraaije, *J. Comp. Chem.* **1997**, *18*, 1463–1472.
- [59] G. Bussi, D. Donadio, M. Parrinello, *J. Chem. Phys.* **2007**, *126*, 014101.
- [60] a) R. E. Schreiber, L. Houben, S. G. Wolf, G. Leitus, Z. L. Lang, J. J. Carbó, J. M. Poblet, R. Neumann, *Nat. Chem.* **2017**, *9*, 369–373; b) E. Nikoloudakis, K. Karikis, M. Laurans, C. Kokotidou, A. Solé-Daura, J. J. Carbó, A. Charisiadis, G. Charalambidis, G. Izzet, A. Mitraki, A. M. Douvas, J. M. Poblet, A. Proust, A. G. Coutsolelos, *Dalton Trans.* **2018**, *47*, 6304–6313.

## Entry for the Table of Contents

$$\text{Affinity} = c_1 + c_2 q/M^2 + c_3 q/M + c_4 V_s^2 + c_5 V_s$$



Atomistic Molecular Dynamics simulations and QSAR-like modeling techniques were applied to establish relationships between the structure of chaotropic polyoxometalate (POM) anions and their affinity towards biological systems. The charge density, size and shape of POMs were identified as important parameters to balance the POM interactions with the protein and with the solvent.